Interbasin and Multiple-Time-Scale Interactions in Generating the 2019 Extreme Indian Ocean Dipole

LEI ZHANG,[a] WEIQING HAN,[a] AND ZENG-ZHEN HU[b]

[a] *Department of Atmospheric and Oceanic Sciences, University of Colorado, Boulder, Colorado*
[b] *NOAA/NWS/NCEP/Climate Prediction Center, College Park, Maryland*

(Manuscript received 29 September 2020, in final form 30 December 2020)

ABSTRACT: An unprecedented extreme positive Indian Ocean dipole event (pIOD) occurred in 2019, which has caused widespread disastrous impacts on countries bordering the Indian Ocean, including the East African floods and vast bushfires in Australia. Here we investigate the causes for the 2019 pIOD by analyzing multiple observational datasets and performing numerical model experiments. We find that the 2019 pIOD was triggered in May by easterly wind bursts over the tropical Indian Ocean associated with the dry phase of the boreal summer intraseasonal oscillation, and it was sustained by the local atmosphere–ocean interaction thereafter. During September–November, warm sea surface temperature anomalies (SSTA) in the central-western tropical Pacific Ocean further enhanced the Indian Ocean's easterly winds, bringing the pIOD to an extreme magnitude. The central-western tropical Pacific warm SSTA was strengthened by two consecutive Madden–Julian oscillation (MJO) events that originated from the tropical Indian Ocean. Our results highlight the important roles of cross-basin and cross-time-scale interactions in generating extreme IOD events. The lack of accurate representation of these interactions may be the root for a short lead time in predicting this extreme pIOD with a state-of-the-art climate forecast model.

KEYWORDS: Climate prediction; Climate variability; Indian Ocean dipole; Interbasin interaction; Intraseasonal oscillation

1. Introduction

The Indian Ocean dipole (IOD) is the dominant mode of Indian Ocean interannual climate variability (Saji et al. 1999; Webster et al. 1999), which is characterized by opposite sea surface temperature anomalies (SSTAs) between the eastern Indian Ocean off the coast of Sumatra and the western tropical Indian Ocean. A positive IOD phase (pIOD) event is associated with warming in the western and cooling in the eastern Indian Ocean, accompanied by surface easterly wind anomalies over the tropical Indian Ocean (Fig. 1). Reversed conditions hold for a negative phase of IOD. The IOD events have profound influences on weather and climate in surrounding countries, including Indian summer monsoon variability (Ashok et al. 2004; Kripalani and Kumar 2004; Gadgil et al. 2004; Ashok and Saji 2007), flood and drought over East Africa and Indonesia (Clark et al. 2003; Black et al. 2003), and temperature and rainfall anomalies in Australia (Cai et al. 2009, 2011; Li et al. 2016; Saji and Yamagata 2003). Through atmospheric teleconnection and interactions with the tropical Pacific Ocean, footprints of the IOD can be found worldwide (Saji and Yamagata 2003; Behera and Yamagata 2003; Izumo et al. 2010; Stuecker et al. 2017; Annamalai et al. 2005; Luo et al. 2010).

The development of the IOD involves large-scale ocean–atmosphere interactions over the tropical Indian Ocean (Murtugudde et al. 2000; Li et al. 2003; Lau and Nath 2004). During a pIOD, the SSTA pattern with warming in the west and cooling in the east drives surface southeasterly/easterly wind anomalies over the eastern/central tropical Indian Ocean through changes in the zonal sea level pressure (SLP) gradient (Lindzen and Nigam 1987) (Fig. S1 in the online supplemental material). The southeasterly wind anomalies along the Sumatra and Java coasts, in turn, cause offshore Ekman currents that diverge from the coasts, allowing the colder subsurface water to upwell to the ocean surface and thus enhance SST cooling. Meanwhile, the anomalous winds enhance the southeasterly trades and surface evaporation, further strengthening the SST cooling signals. Along the equator, easterly wind components cause westward surface currents, transporting the warm pool water from the eastern Indian Ocean westward and amplifying the SSTA zonal gradient; concurrently, easterly wind anomalies induce Ekman divergence (upwelling) along the equator, and Ekman convergence (downwelling) off the equator. The upwelling (downwelling) signals propagate eastward (westward) as equatorial Kelvin (Rossby) waves, further enhancing the east–west dipole pattern of SSTA (Gualdi et al. 2003; Feng and Meyers 2003; Shinoda et al. 2004; Huang and Shukla 2007b).

In addition to the local ocean–atmosphere interaction, El Niño–Southern Oscillation (ENSO), which is the dominant mode of interannual climate variability on the planet (McPhaden et al. 2006; Huang and Shukla 2007a,b; Huang and Kinter 2002), can also play a role in the IOD formation (Saji et al. 2006; Allan et al. 2003; Krishnamurthy and Kirtman 2003; Annamalai et al. 2003; Meyers et al. 2007; Huang and Shukla 2007b; Wang et al. 2019; Huang and Kinter 2002). During El Niño (the positive phase of ENSO), convection (rainfall) is suppressed over the

Supplemental information related to this paper is available at the Journals Online website: https://doi.org/10.1175/JCLI-D-20-0760.s1.

Corresponding author: Lei Zhang, lezh8230@colorado.edu

DOI: 10.1175/JCLI-D-20-0760.1

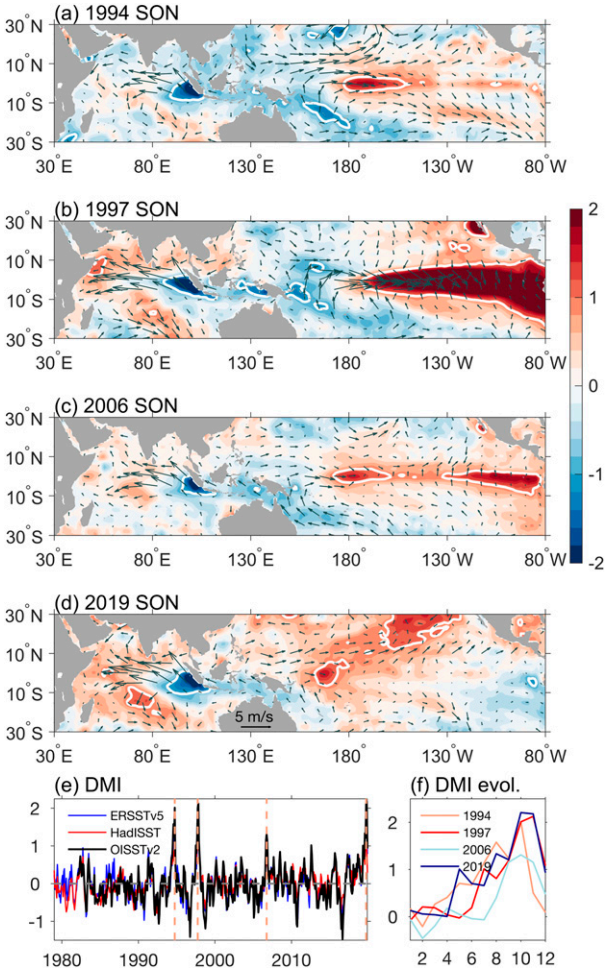

FIG. 1. Extreme pIODs during the satellite era, showing SSTAs (°C) during SON (the peak season of IOD) in (a) 1994, (b) 1997, (c) 2006, and (d) 2019 from OISSTv2 data. White lines denote the −1° and 1°C contours. Vectors represent surface wind anomalies ($m\,s^{-1}$). (e) Time evolution of the DMI (°C), defined as differences of SSTAs averaged over 50°–70°E, 10°S–10°N and 90°–110°E, 10°S–0°. The blue, red, and black lines are for ERSSTv5, HadISST, and OISSTv2, respectively. (f) Evolution of monthly DMI (°C) from OISSTv2 during the extreme pIOD events in 1994 (orange), 1997 (red), 2006 (green), and 2019 (blue). The peak time (SON) of the four events is denoted by the vertical orange dashed lines in (e).

western tropical Pacific warm pool and the "Maritime Continent" (Fig. S2 in the online supplemental material), leading to higher SLP in the region (Fig. S1). The zonal SLP gradient induces surface easterly wind anomalies over the tropical Indian Ocean and thereby contributes to the generation and development of the pIOD.

Since the early 1980s when satellite observations became available, three extreme pIOD events have occurred in 1994, 1997, and 2006 (Fig. 1), which have been extensively studied (Saji et al. 1999; Webster et al. 1999; Behera et al. 1999; Vinayachandran et al. 1999; Horii et al. 2008). The three extreme pIOD events are all accompanied by El Niño, although by different flavors of ENSO with major warm SSTA located at different regions of the tropical Pacific Ocean; whereas both 1997 and 2006 are classified as eastern Pacific El Niños, 1994 is a central Pacific El Niño event (Yu et al. 2012). Using an atmospheric general circulation model (AGCM) forced with observed Pacific SSTAs in 1994, 1997, and 2006, we indeed find that the El Niño events induce easterly wind anomalies over the tropical Indian Ocean and thereby strengthen the three historical extreme pIOD events (Fig. S3 in the online supplemental material).

In autumn 2019, another extreme pIOD occurred with the peak value of the monthly dipole mode index (DMI; defined as the west–east SST gradient in the tropical Indian Ocean) close to 2.2°C (Fig. 1f). This makes the 2019 pIOD the strongest event during the satellite era since the early 1980s (Fig. 1e). Meanwhile, positive SSTAs have been observed in the central tropical Pacific—particularly the central-western Pacific west of the date line—in 2019, with the center of warming being shifted farther west relative to that during the other three extreme pIOD events (Fig. 1). This 2019 extreme pIOD caused disastrous impacts on countries nearby. For instance, rainfall at the horn of East Africa was up to 300% above average in October–November 2019 (Famine Early Warning Systems Network report; https://reliefweb.int/report/south-sudan/east-africa-food-security-outlook-high-food-assistance-needs-persist-food), when the pIOD attained its peak. The excess rainfall resulted in severe flooding in the region that killed hundreds and affected more than 2.8 million people (United Nations Office for the Coordination of Humanitarian Affairs report; https://reliefweb.int/report/south-sudan/eastern-africa-region-regional-flood-snapshot-november-2019). Meanwhile, massive bushfires raged through Australia due to the warm and dry conditions there, which are typically observed during pIOD events and therefore are likely associated with the 2019 pIOD. The 2019 pIOD also contributed to the extremely warm conditions over East Asia during the winter season of 2019/20 (Doi et al. 2020a). Therefore, understanding the generation, development, and predictability of the 2019 extreme pIOD event has large societal benefits.

2. Data and method

a. *Observational datasets*

In this study, we use the monthly SST data from the Hadley Centre Sea Ice and SST (HadISST; Rayner et al. 2003) and Extended Reconstructed SST, version 5 (ERSSTv5; Huang et al. 2017), during 1979–2019 and National Oceanic and Atmospheric Administration (NOAA) Optimum Interpolation SST, version 2 (OISSTv2; Reynolds et al. 2002) during 1982–2019 to analyze the tropical Indian Ocean and Pacific SSTAs during the extreme pIODs. To analyze the seasonal variations of the tropical Indo-Pacific atmospheric conditions, we use monthly surface wind, SLP, and precipitation data from the fifth major global reanalysis produced by the European Centre for Medium-Range Weather Forecasts (ERA5; Hersbach et al. 2019), and outgoing longwave radiation (OLR) data from

NOAA Interpolated OLR (Liebmann and Smith 1996). To examine the subseasonal variations and their contributions to the 2019 pIOD, we analyze daily OISSTv2 and ERA5 surface wind data, for which we remove the first three harmonics of the daily climatology to obtain the anomaly fields. To examine the oceanic wave processes, we also analyzed satellite-derived daily sea surface height (SSH) data during 1993–2019 obtained from the Copernicus Marine Environment Monitoring Service.

To examine the Madden–Julian oscillation (MJO) activities, we use an MJO index from the Climate Prediction Center of the National Centers for Environmental Prediction (NCEP) that is based on an extended empirical orthogonal function analysis (available at https://www.cpc.ncep.noaa.gov/products/precip/CWlink/daily_mjo_index/mjo_index.shtml). For comparison, we also use the OLR-based MJO index (OMI; Kiladis et al. 2014; available at https://www.esrl.noaa.gov/psd/mjo/mjoindex/).

To select the extreme pIOD events during the satellite era, we use the DMI (Saji et al. 1999), which is differences of SSTAs averaged over 50°–70°E, 10°S–10°N and 90°–110°E, 10°S–0°. The extreme pIODs are defined as the years when the monthly DMI during the peak season (September–November) exceeds 2 standard deviations of the index (~1°C). Four pIOD events are selected: 1994, 1997, 2006, and 2019.

To explore the causes for the SSTAs associated with the 2019 pIOD, we examine the oceanic mixed layer (OML) heat budget. Following Huang et al. (2010), the heat budget equation of OML is

$$T_t = Q_u + Q_v + Q_w + Q_{zz} + Q_q,$$

where T_t is the time tendency of the OML temperature; Q_u and Q_v represent the zonal and meridional advection, respectively; Q_w and Q_{zz} are the vertical entrainment and vertical diffusion, respectively; and Q_q is the net surface heat flux. Monthly heat budget terms are diagnosed using outputs from the NCEP Global Ocean Data Assimilation System (Ji et al. 1998; Huang et al. 2010), in which the mixed layer depth is defined as the depth at which the density difference from the surface reaches 0.125 kg m^{-3}. Note that there are relatively large biases in the Q_w and Q_{zz} terms for the coastal area because of the limited resolution, and therefore their contributions to the cold pole of the pIOD in the eastern tropical Indian Ocean may not be captured well.

b. CFSv2 forecasts

To assess the prediction skill of IOD, we verify the real-time predictions of the Climate Forecast System, version 2 (CFSv2; Xue et al. 2013; Saha et al. 2014), which is a global coupled climate model and provides real-time operational forecasts at NCEP. In this study, we analyze the 9-month predictions starting from January through September 2019, and the forecasts were initiated with 40-day initiation conditions (from the 10th of the target month going backward to the previous month for 40 days), and four forecasts each day (0000, 0600, 1200, and 1800 UTC). Hence, we use 160 ensemble members to construct the ensemble mean in each month.

c. Atmosphere model

To investigate the impact of the Pacific Ocean forcing on the tropical Indian Ocean through the atmospheric bridge, we perform two sets of sensitivity experiments using the AGCM ECHAM4.6 (Roeckner et al. 1996) from the Max Planck Institute in Hamburg, Germany. The model horizontal resolution is approximately 2.8°, with 19 vertical levels. For each experiment, the model is integrated for 40 years, and the first four years are discarded given that it takes a few years to reach the model equilibrium. Hence, we have a 36-member ensemble for all the experiments.

In addition to the control run, which is forced with monthly SST climatology, we perform two sets of experiments, forced with realistic and idealized Pacific SSTA, respectively. In the first set of experiments, we add the September–November averaged tropical Pacific SSTA (30°N–30°S) during the extreme pIODs to the monthly SST climatology throughout the year. We perform three experiments, forced with observed 1994/2006 (average of the two events, since both years exhibit similar central tropical Pacific warming anomalies), 1997, and 2019 Pacific SSTAs, respectively.

In the second set of experiments, we force the model with idealized SST warming anomalies centered at the central Pacific [CP-I (140°E–170°W, 10°S–10°N) and CP-II (170°E–140°W, 10°S–10°N)] and the eastern tropical Pacific (EP; 160°–80°W, 10°S–10°N). To examine whether the western (WNP; 125°–165°E, 10°–30°N) and eastern (ENP; 160°–120°W, 10°–30°N) North Pacific SST warmings in 2019 also contribute to the development of the extreme pIOD, we perform two additional experiments by adding idealized SST warming in those two regions separately. The idealized SST warming has a 1°C peak warming at the center and gradually decays to 0°C toward the edges. Since the eastern Pacific warming in 1997 is much stronger when compared with those in the other extreme pIOD years (Fig. 1), we perform another additional experiment with 2°C peak warming centered in the eastern tropical Pacific region.

d. Linear ocean model

To investigate the relative roles of remote and local wind forcings in affecting the coastal ocean off the Sumatra and Java coasts, we use a linear continuously stratified ocean model (McCreary 1981; Han 2005), forced with differences of Indian Ocean surface winds between the CP-I warm SSTA and the control run of AGCM experiments. The model domain is approximately 30°–120°E, 35°S–35°N. The ocean model experiment started from a state of rest with a realistic background stratification and 25 baroclinic modes. The ocean bottom is assumed to be flat with a depth of 4000 m, and the horizontal resolution is 0.5°. The model is integrated for 60 months, and the last 48 months of results are analyzed.

3. The extreme pIOD in 2019

Here we examine the evolution of the extreme pIOD in 2019 (Figs. 2 and 3) and explore the associated physical mechanisms. Observations show that the 2019 pIOD starts to develop in May (Figs. 1f and 2b), as seen from the dramatic increase in

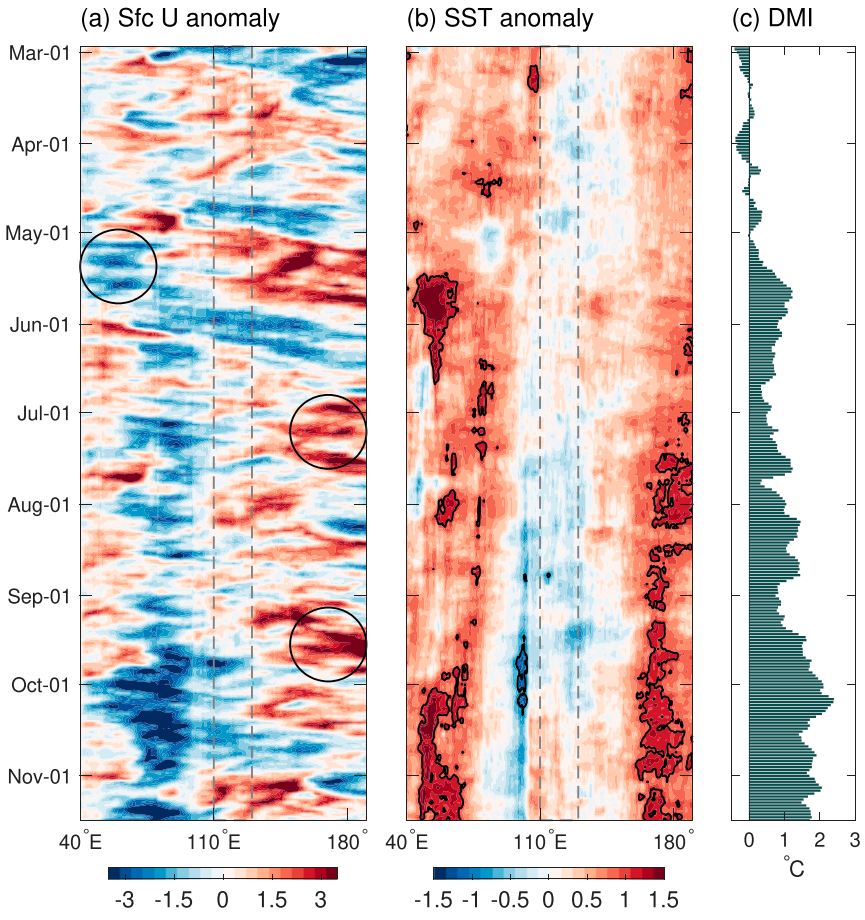

FIG. 2. Evolution of the 2019 extreme pIOD, showing Hovmöller diagrams of daily (a) surface zonal wind anomalies averaged between 15°N and 15°S from ERA-5 ($m\,s^{-1}$) and (b) SSTAs from OISSTv2 (°C) averaged between 10°N and 10°S, along with (c) the daily DMI from OISSTv2. Contours in (b) represent 1° or −1°C of SSTA. The vertical dashed lines in (a) and (b) denote 110° and 130°E, which represent the location of the Maritime Continent.

the DMI with an amplitude larger than 1°C in mid-May, which is mainly associated with strong warming in the western tropical Indian Ocean—the western pole of the pIOD (Fig. 2b). We also find warm SSTAs in the tropical Indian Ocean before May (Fig. 2b), which are mainly located at the southern tropical Indian Ocean in the so-called Seychelles-Chagos thermocline ridge region (Fig. 6), and therefore these warm signals may not be part of the pIOD signals. An OML budget analysis reveals that the Indian Ocean SSTA dipole in May is primarily caused by changes in the surface heat fluxes (Fig. 4a). Consistently, the Hovmöller diagram of zonal wind anomalies (Fig. 2a) shows that episodic easterly wind bursts (EWBs) prevail over the western and central Indian Ocean basin in the early and mid-May, weakening the westerly monsoon circulation, reducing the surface turbulent heat loss from the ocean and thereby causing warm SSTA in the pIOD's western pole. Meanwhile, the EWBs also cause an oceanic upwelling Kelvin wave in the central tropical Indian Ocean that subsequently propagate eastward (Fig. 3). Although the associated zonal SSH gradient anomaly along the Indian Ocean equator is weak averaged in May (Fig. 3), our analysis of temporal evolution shows a delayed impact of the EWBs on SSH anomalies and SSTA in the eastern pole of the pIOD from late May to mid-June, reducing SSH anomalies and SSTA in the region (Figs. 2a,b, 3, and 5). This is consistent with the further strengthening of the cold pole in late May to early June (Fig. 6). However, since the OML heat budget has relatively large biases in the coastal region, it may not capture the role of oceanic Kelvin waves in enhancing the cold pole (Fig. 4b). Also note that Fig. 2 shows SSTA averaged in the tropical Indian Ocean between 10°S and 10°N, which underestimates the amplitude of the IOD cold pole that is mainly confined in the coastal region (Fig. 6).

The EWBs are associated with prominent dry anomalies over the eastern tropical Indian Ocean, and both the wind and rainfall anomalies exhibit evident northward propagation (Fig. 5). In late May, the EWBs and the associated dry anomalies reach the north Indian Ocean; meanwhile, wet anomalies accompanied by westerly wind anomalies appear over the tropical Indian Ocean. These northward-propagating intraseasonal variabilities have been extensively studied, and they are referred

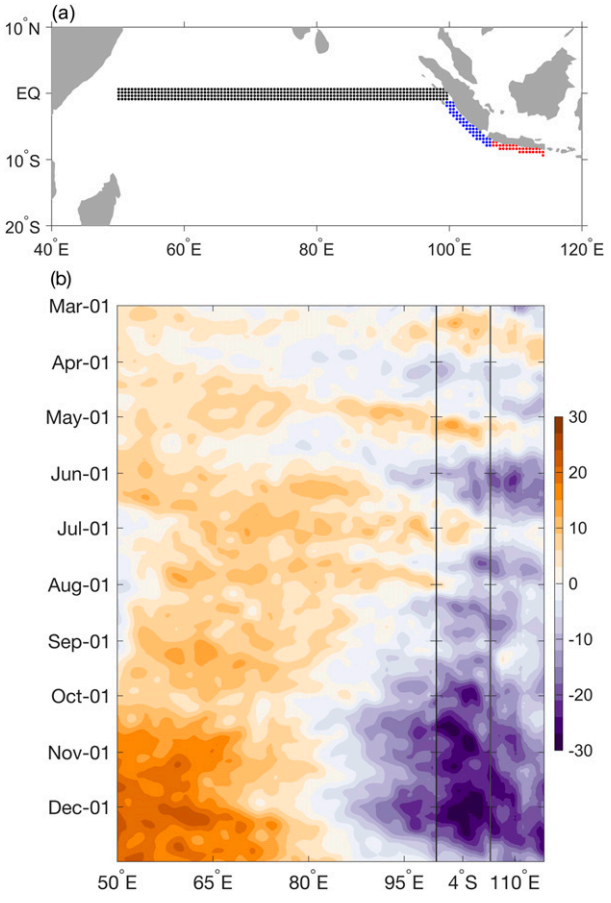

FIG. 3. (a) The three regions used to calculate the SSH anomalies (cm). In regions 1 and 3 (black and red dots, respectively) SSH is averaged meridionally, and in region 2 (blue dots) SSH is averaged in the direction perpendicular to the Sumatra coasts. (b) Evolution of SSH anomalies in the three regions denoted in (a).

to as the boreal summer intraseasonal oscillation (BSISO; Lawrence and Webster 2002). Hence, the initiation of the pIOD in May 2019 is triggered by the EWBs associated with the dry phase of the BSISO, which cause dipole-like SSTA in the tropical Indian Ocean with a few days lag (Fig. 6) through changing the surface heat fluxes.

Once the EWBs induce east–west dipole-like SSTAs in the tropical Indian Ocean in May, local positive atmosphere–ocean feedback kicks off, which sustains the development of both SST and wind anomalies associated with the pIOD in the following months. Indeed, the DMI remains positive, and easterly wind anomalies prevail throughout June and July, despite slightly weaker amplitudes compared to May. From late July to October, the pIOD exhibits a steady intensification with a temporary weakening in early September (Figs. 1f and 2c), and the zonal SSH gradient strengthens (Fig. 3). The monthly DMI increases from 0.7°C in July to 2.2°C in October when the pIOD peaks, making it the strongest event in the past ~40 years. Consistently, easterly wind anomalies intensify and occupy the entire equatorial basin in October (Fig. 2a), which also cause equatorial and coastal upwelling Kelvin waves propagating from the central equatorial Indian Ocean to the Sumatra and Java coasts (Fig. 3). The temporary interruption of the pIOD development in early September is due to the influences of the MJO (Madden and Julian 1971) (Fig. S4 in the online supplemental material). As revealed by multiple MJO indices, a wet MJO event originated from the tropical Indian Ocean in late August and subsequently propagate eastward into the tropical Pacific. The wet MJO is associated with strong intraseasonal westerly wind anomalies, which temporarily disrupt the growth of the 2019 pIOD.

4. Pacific contribution to the extreme pIOD

The unprecedented intensity of the 2019 pIOD is due to a combination of the large initial warming in the western pole in May and the persistent intensification during August–October. While the former is caused by a strong dry BSISO event, what causes the intensification of easterly wind anomalies and the pIOD in August–October 2019 demands further investigation. Previous studies have shown that active interbasin interactions between the tropical Indian and Pacific Oceans play important roles in affecting tropical climate variability (Wang 2019; Cai et al. 2019; Zhang and Han 2018; Luo et al. 2012; Han et al. 2014; Zhang et al. 2019). Note that the development of the 2019 pIOD in boreal summer and autumn is accompanied by persistent positive SSTAs in the central tropical Pacific, with a maximum magnitude exceeding 1°C to the west of the date line where the mean SST exceeds 29°C (Figs. 1d and 2b). This warming center is shifted farther to the west compared to that during the other historical extreme pIODs (Fig. 1).

Do the warm SSTAs within the central-western Pacific contribute to the development of the 2019 pIOD? To answer this question, we perform AGCM experiments forced with observed September–November (SON) mean SSTAs of 2019 in the tropical Pacific (Figs. S3e,f in the online supplemental material). Results show that the central-western tropical Pacific warming in 2019 shifts the tropical Pacific convection center eastward and thereby suppresses convection over the Maritime Continent. Thus, the warm SSTAs in the central-western tropical Pacific indeed enhance the easterly wind anomalies over the tropical Indian Ocean, contributing to the pIOD development in 2019. Interestingly, we note that the Pacific SSTA also induces cyclonic wind anomalies over the western North Pacific (Fig. S3f), which agrees with the observations (Fig. S1d in the online supplemental material) and the associated northerly wind anomalies over East Asia have been suggested to contribute to the severe drought in East China in 2019 (Ma et al. 2020). This further validates our model results.

Hence, the development of the 2019 pIOD and the three historical extreme pIOD events are all influenced by the tropical Pacific forcing. However, the tropical Pacific warming anomalies are centered at different locations during the four pIOD events. Are the responses in the tropical Indian Ocean sensitive to the location of the tropical Pacific warming? To explore the relative roles of the Pacific SSTAs at different locations in the development of the four extreme pIOD events, we conduct another set of AGCM experiments using idealized

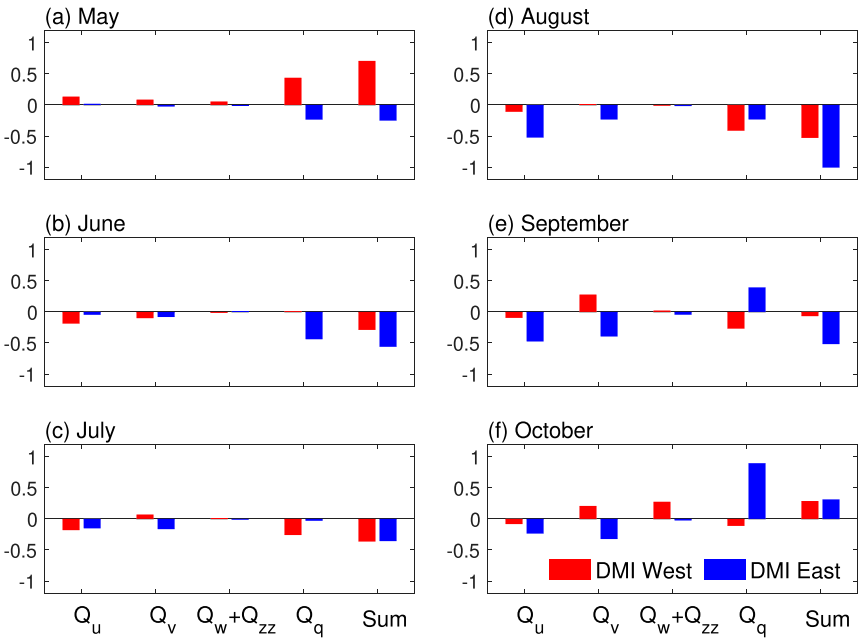

FIG. 4. Mixed layer heat budget (°C month^{-1}) for (a) May, (b) June, (c) July, (d) August, (e) September, and (f) October 2019 for the western (red; 50°–70°E, 10°S–10°N) and eastern (blue; 90°–110°E, 10°S–0°) poles of the DMI. Shown are horizontal advection Q_u, meridional advection Q_v, vertical entrainment and diffusion ($Q_w + Q_{zz}$), and surface heat flux contributions Q_q. Sums of these terms are also shown.

SSTA forcing (Fig. 7). Positive SSTAs with the same 1°C maximum warming at the center are specified for different areas of the Pacific basin to represent the observed Pacific SSTAs during the four extreme pIODs. Here we use CP-I to represent the location of the central-western tropical Pacific warming during 2019, which is to the west of the date line; as a comparison, CP-II represents the location of central Pacific El Niños during 1994 and 2006, with the warming center located to the east of the date line. Results show that the anomalous warming in the tropical Pacific induces easterly wind anomalies in the tropical Indian Ocean, no matter whether the warming is in the CP-I, CP-II, or eastern tropical Pacific region (Figs. 7a–c). The role of the Pacific warm SSTA in causing tropical Indian Ocean easterly wind anomalies is mainly through shifting the Pacific convection center eastward and thereby causing below-average rainfall over the Maritime Continent (Fig. S5 in the online material), which in turn induces atmospheric Rossby waves to its west over the Indian Ocean manifested as a pair of low-level anomalous anticyclones straddling the equator that correspond to strong easterly wind anomalies in the tropics.

Interestingly, the intensities of the Indian Ocean easterly wind anomalies driven by the tropical Pacific SSTAs depend critically on the location of the SSTA forcing. While warming in the CP-I region produces the strongest wind anomalies in the equatorial Indian Ocean (Fig. 7a), impacts of the same degree of warming in CP-II and eastern Pacific cold tongue region on the Indian Ocean are relatively weak (Figs. 7a–c; see also Fig. S5). This is due to the nonlinear dependence of the tropical rainfall, which is the heating source that drives changes in atmospheric circulation, on the mean state SST (Gadgil et al. 1984; Graham and Barnett 1987; Waliser and Graham 1993)—the increases of rainfall per degree SST warming (mm day^{-1} °C^{-1}) are higher in the region where the background SST is higher. Indeed, the positive rainfall anomalies in the tropical Pacific caused by warming in CP-I region are larger than those caused by warming in CP-II region and eastern tropical Pacific (Fig. S5). Therefore, the longitudinal location of tropical Pacific warm SSTA in 2019 provides the most favorable condition for the development of the pIOD.

Note that both the remote equatorial easterlies and the local alongshore southeasterlies off Sumatra and Java coasts can induce coastal upwelling in the eastern pole of the pIOD and thereby favor the pIOD development. However, while the CP-I warming induces strong easterly wind anomalies across the equatorial Indian Ocean that enhance upwelling in the eastern pole via exciting eastward-propagating equatorial Kelvin waves, it causes weak but southwesterly winds off Sumatra and Java coasts, which reduce upwelling and weaken the cold SSTA there (Fig. 7a). To assess the relative importance of remote versus local wind anomalies induced by CP-I warm SSTA in affecting the cold SSTA in the east pole of the pIOD, we use the wind anomalies induced by CP-I warm SSTA to force a linear ocean model. The results show that the remote equatorial winds dominate the local winds in driving upwelling cooling in the eastern pole, causing east–west dipole-like SSH anomalies that favor enhancing the pIOD (Fig. 8). Indeed, observations also show eastward propagating Kelvin wave signals originated from

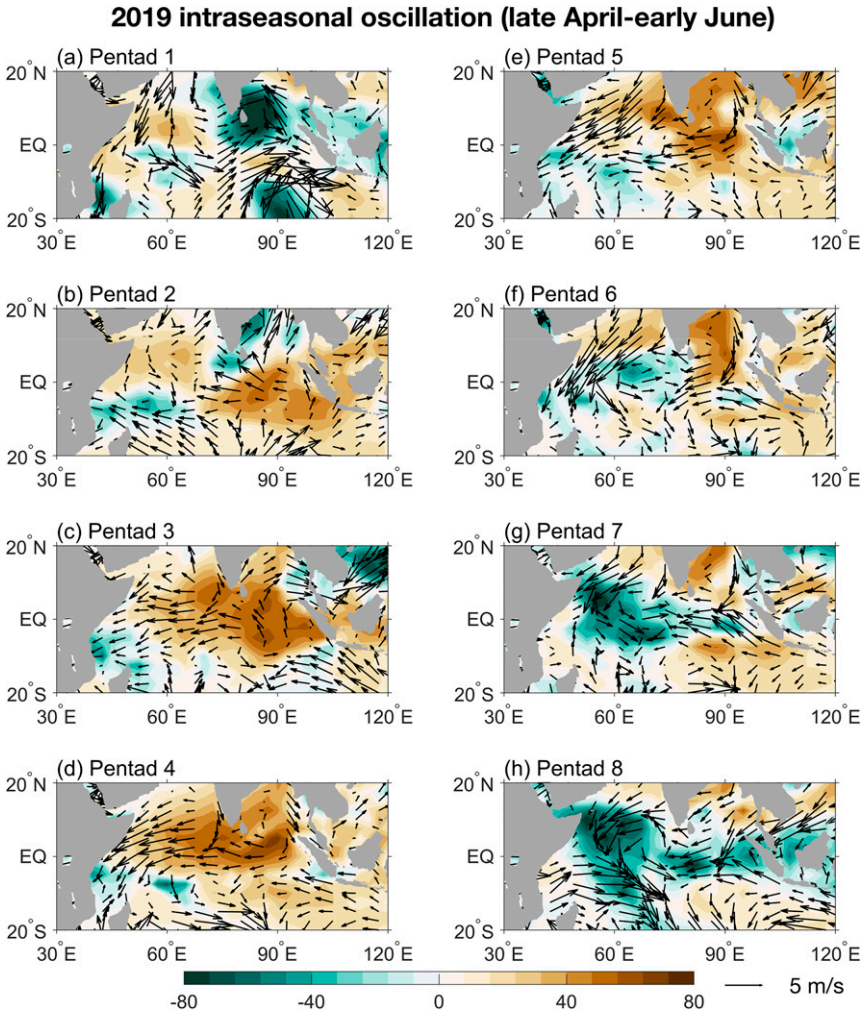

FIG. 5. Pentad mean OLR (shading; W m^{-2}) and surface wind (vectors; m s^{-1}) anomalies from 26 Apr to 4 Jun 2019; 20–90-day filtered intraseasonal anomalies show very similar results.

the central equatorial Indian Ocean in October 2019 (Fig. 3). These results further support the prominent role of the CP-I warming in enhancing the pIOD, despite the weak alongshore wind response over the eastern Indian Ocean.

Given that the eastern Pacific positive SSTAs during the 1997–98 El Niño are much stronger than those in the other three extreme pIODs (Fig. 1), we performed one additional sensitivity experiment by doubling the warming magnitude in the eastern tropical Pacific (Fig. 7d). Results show that the Indian Ocean easterly wind anomalies driven by the stronger eastern Pacific warm SSTA with 2°C at the center are as strong as those induced by the CP-I warm SSTA with 1°C at the center (Figs. 7a,d). Consistently, the 1997 pIOD is the second strongest event during the satellite era after the 2019 pIOD.

We also note that, in 2019, weak positive SSTAs are seen in the western North Pacific south of Japan, and strong SSTAs are shown in the eastern North Pacific east of the Hawaiian Islands, while these warming signals are absent in the other three historical extreme pIOD years (Fig. 1). We then examine if those SSTAs also contribute to the 2019 pIOD by performing model experiments with idealized warm SSTAs added in the two regions separately. Results show that although the western North Pacific warming induces easterly wind anomalies over the tropical Indian Ocean, its impact is much weaker compared with that of the tropical Pacific warm SSTAs (Figs. 7a–e). The eastern North Pacific warm SSTA almost does not affect the Indian Ocean winds (Fig. 7f). Consequently, it is the warming in the central-western tropical Pacific that enhances the 2019 pIOD and makes it the strongest pIOD in the past ~40 years.

We note that the central Pacific warm SSTA can be found as early as winter 2018/19 (Doi et al. 2020b), but it decays significantly in spring 2019 and then reintensifies since July 2019 (Fig. 2b). To explore the causes for the strengthening of the central-western tropical Pacific warm SSTA in the summer and autumn of 2019, we carry out a budget analysis of mixed layer temperature (figure not shown). Results show that the SST warming tendency mainly occurred in July and September, and is primarily caused by surface heat flux anomalies, with some

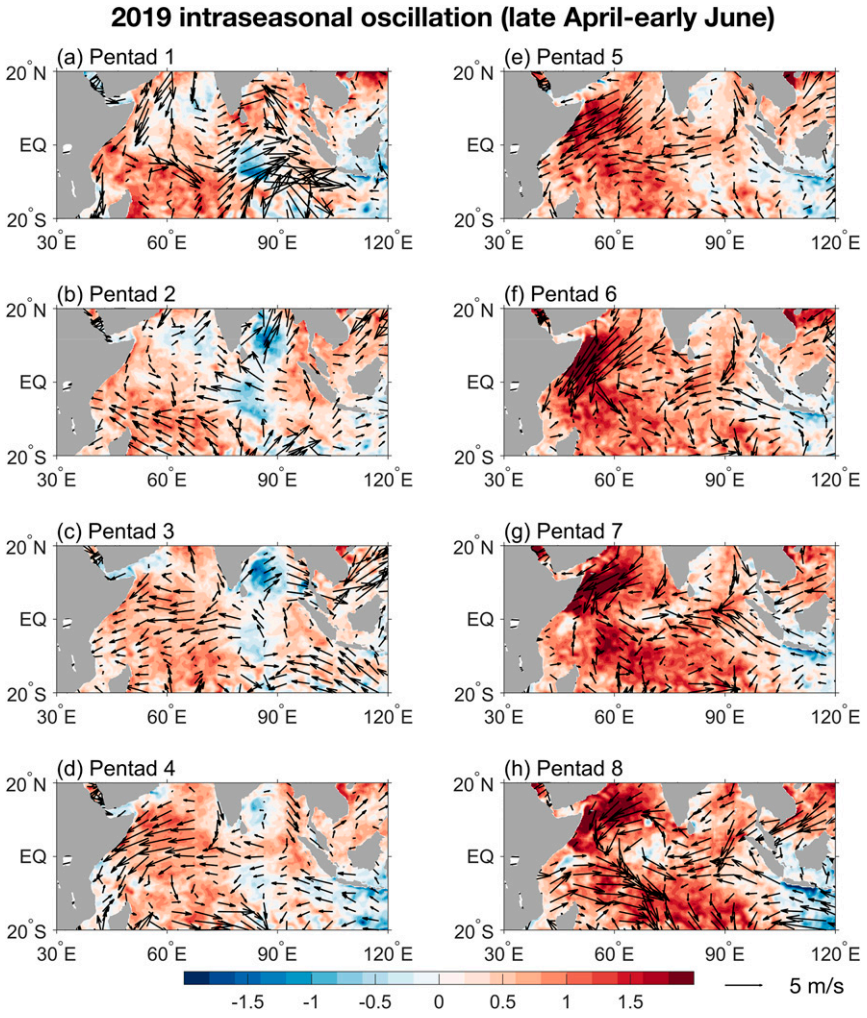

FIG. 6. As in Fig. 5, but for pentad-mean SST anomalies (°C).

contribution from the reduced upwelling and meridional heat advection anomalies. These atmospheric and oceanic anomalies are closely related to the westerly wind anomalies in the region (Fig. 2a), which weaken the wind speed and the oceanic upwelling. Indeed, the pentad-mean anomalies in the two months show intraseasonal westerly wind anomalies that sustain for 3–4 pentads, which are followed by SST warming tendency (not shown). As shown in various MJO indices, the westerly wind bursts in the western tropical Pacific that further strengthen CP-I warm SSTA since July 2019 are associated with two wet MJO events originated from the tropical Indian Ocean (Fig. S4 in the online supplemental material). Hence, the interbasin and multiple-time-scale interactions play a crucial role resulting in the 2019 extreme pIOD.

5. Prediction of the 2019 extreme pIOD

Given that the 2019 extreme pIOD had large societal impacts, it is meaningful to evaluate the performance of climate models in predicting this event. Here we verify the real-time forecasts from the NCEP CFSv2 (Xue et al. 2013; Saha et al. 2014). The 9-month forecasts starting from January through September 2019 generally call a quick decay of the pIOD in 2019 (Fig. 9), and therefore, it is unsuccessful to predict the extreme pIOD event. Even with initialization in July, which is close to the pIOD peak in October, the forecasts still severely underestimate the DMI amplitude (Fig. 9h). Only when the forecast is initialized in August that the predicted DMI is comparable to the observation (Fig. 9i).

One of the reasons that the model is unsuccessful in predicting the 2019 extreme pIOD is likely due to the interruption of subseasonal activities, which is unpredictable beyond a couple of weeks (Lim et al. 2018). The subseasonal variabilities associated with the BSISO and MJO activities are considered as noises that degrade the predictability of monthly and seasonal climate. As shown above, the BSISO/MJO activities are active in 2019 and play a crucial role in triggering the pIOD and the central tropical Pacific warm SSTA, which

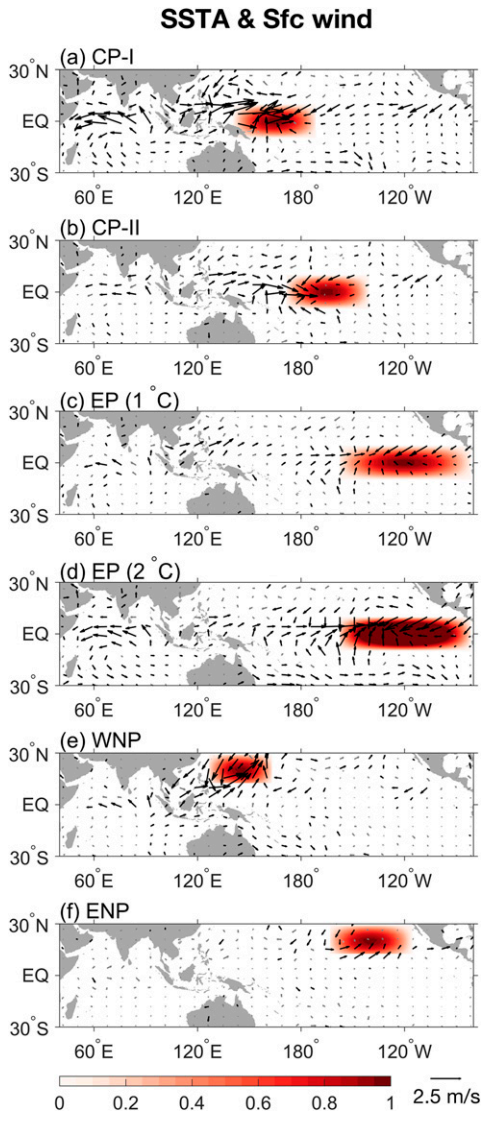

FIG. 7. Idealized SST forcing experiments, showing idealized SST warming anomalies (shading; °C) and simulated SON averaged surface wind anomalies (vectors; m s^{-1}). The maximum SST warming anomaly is 1°C except for (d), in which the maximum warming is 2°C. The forcing is centered at (a) the CP-I, (b) the CP-II, (c),(d) the eastern equatorial Pacific (EP), (e) the western North Pacific (WNP), and (f) the eastern North Pacific (ENP). Black vectors denote wind anomalies that are statistically significant at the 90% confidence level.

subsequently enhances the pIOD. Consequently, the model's ability in predicting the development of the pIOD in 2019 is limited.

We further note that for the forecasts starting in September, the ensemble mean DMI is close to the observed value, but there exists a relatively large spread (Fig. 9i); some members overestimate the DMI while some members underestimate it. A comparison between these two categories shows

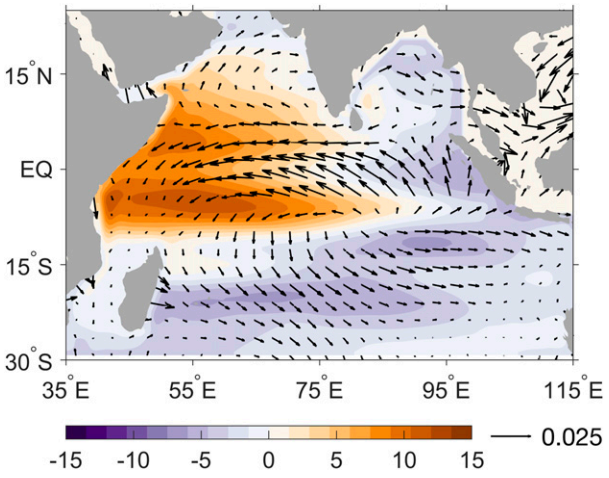

FIG. 8. SSH anomalies (shading; cm) in a linear ocean model forced with SON surface wind stress anomalies (vectors; N m^{-2}) in CP-I atmosphere model experiments relative to the control run.

remarkable differences in the tropical Pacific SST; the mean of the ensemble members that predict a stronger pIOD also predicts larger SSTAs in the central-western tropical Pacific, as well as in the western and eastern North Pacific (Fig. 10). Since the AGCM sensitivity experiments have suggested that warm SSTA in the central-western tropical Pacific is the most efficient driver for easterly wind anomalies in the tropical Indian Ocean that strengthen the pIOD (Fig. 7), the real-time forecast results (Fig. 10) provide further evidence for the important role of the central-western tropical Pacific warming in the formation of the 2019 extreme pIOD.

6. Summary and discussion

An unprecedented positive IOD event (pIOD) occurred in 2019, which has caused severe climatic impacts on countries nearby. By combining observational analysis and numerical model experiments, we investigate the genesis, evolution, and prediction of this extreme event. We find that the 2019 extreme pIOD was triggered by easterly wind bursts (EWBs) over the tropical Indian Ocean in May, which is associated with the suppressed/dry phase of BSISO (Fig. 11a). The EWBs caused warm SST anomalies (SSTAs) in the western pole of the pIOD (by reducing surface wind and evaporative cooling) and, to a lesser degree, cold SSTAs in the eastern pole. The east–west SST gradient kicked off the local atmosphere–ocean coupling that sustains its development thereafter. From August onward, the pIOD further intensified and reached its peak in October. In addition to local positive air–sea feedback, the warm SSTAs in the central-western tropical Pacific (west of the date line) generated easterly wind anomalies in the equatorial Indian Ocean, enhancing the pIOD and making it the strongest event during the satellite era since the 1980s (Fig. 11b). The warm SSTA in the central-western Pacific mainly developed since

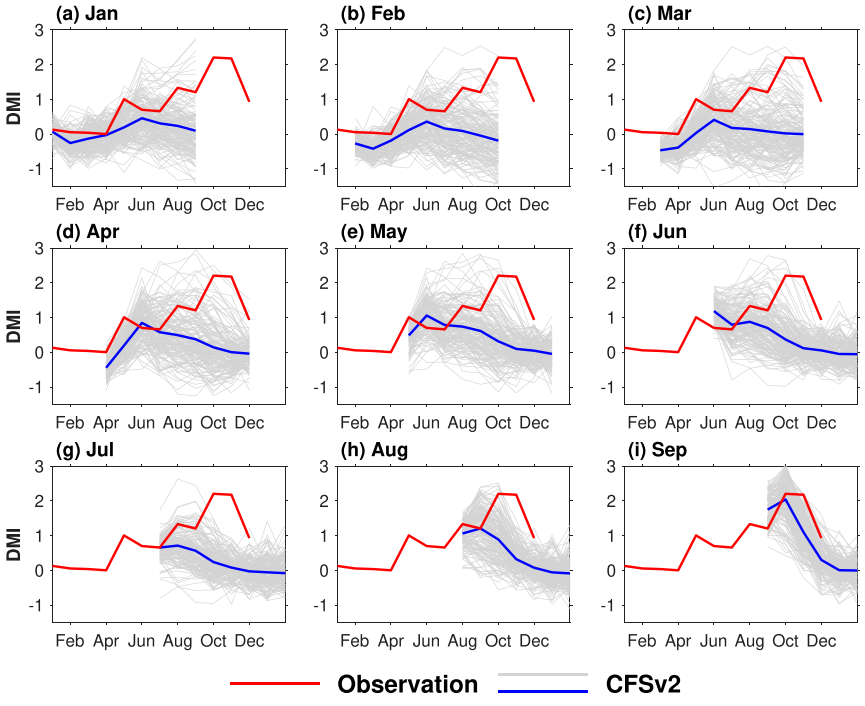

FIG. 9. CFSv2 predicted time evolution of monthly DMI (°C) of the 2019 extreme pIOD. The red curve is the observations that are based on OISSTv2. Gray curves are 160-member ensemble of the 9-month prediction, and the blue curve is the ensemble mean results. The predictions use initial conditions from January to September and the month before (see section 2), as labeled.

July 2019 as a result of two consecutive MJO events originating from the tropical Indian Ocean. In addition to the dry BSISO event in May 2019, Du et al. (2020) recently suggested that the westward propagating oceanic downwelling Rossby waves in the southern tropical Indian Ocean could also help to trigger the 2019 pIOD through inducing warm SSTAs in the western basin that drive easterly wind anomalies over the tropical Indian Ocean.

When compared with the historical extreme pIOD events of 1994, 1997, and 2006 in the past 40 years, the 2019 pIOD is unique in a few aspects: It is accompanied by the tropical Pacific warm SSTAs located farther to the west, with the center located within the warm pool region compared to the other three events; it is the strongest in magnitude as measured by the dipole mode index with large anomalies in both the west and east poles; and it is triggered by strong EWBs. While westerly wind bursts associated with the active/wet phase of MJO have been shown to terminate pIOD and initiate El Niño (Rao and Yamagata 2004; Han et al. 2006), roles of easterly wind anomalies over the tropical Indian Ocean associated with the suppressed/dry phase of BSISO and MJO in affecting pIOD have largely been neglected. Importantly, our results show that tropical Indian Ocean responses to Pacific SSTA are sensitive to the location of the SSTA. The warm SSTA centered in the central-western tropical Pacific to the west of the date line, like 2019, is the most efficient driver of the extreme pIOD compared with warming farther to the east (i.e., central and eastern tropical Pacific) as in the other three extreme pIOD events. A recent study by Lu and Ren (2020) argued that the interhemispheric pressure gradient (IHPG) anomaly associated with high pressure anomalies over the south Indian Ocean and low pressure anomalies over the Philippine Sea may help strengthen the southeasterly wind anomalies over the eastern tropical Indian Ocean and thereby contributed to the growth of the 2019 pIOD. Interestingly, we note that our AGCM experiments forced with the 2019 Pacific SSTA also reproduces a somewhat similar SLP anomaly pattern (Fig. S3 in the online supplemental material). Hence, the IHPG, which is suggested to contribute to the formation of the 2019 extreme pIOD, could be partly associated with the central Pacific warm SSTA.

In addition to the conditions associated with the intraseasonal to interannual variations, the multidecadal and centennial trend in the Indian Ocean SST also seems favorable for the development of the 2019 pIOD. For instance, Wang et al. (2020) found that the strengthening trend of the southerly winds off the Sumatra coasts in the past few decades may have contributed to the 2019 pIOD by further reinforcing the pIOD-related alongshore wind anomalies in the eastern basin, which subsequently enhances the cold pole of the 2019 pIOD. Such long-term wind changes could be associated with the anthropogenic global warming effect. Indeed, Cai et al. (2014) projected more frequent extreme pIOD events under global warming due to mean state changes that are more conducive to the development of pIOD events.

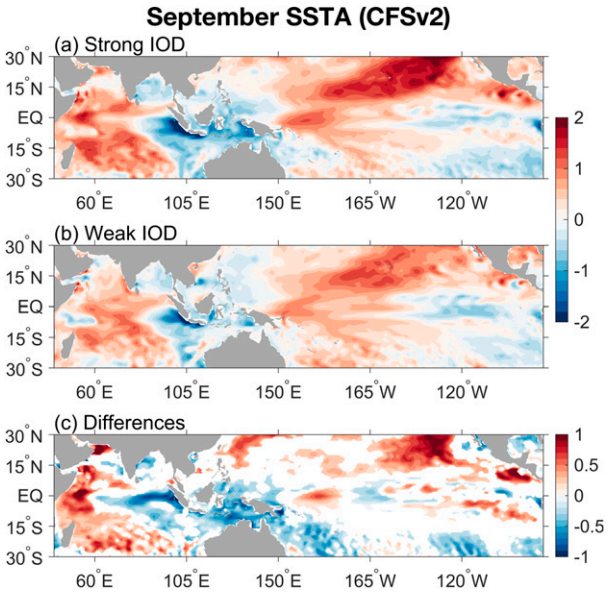

FIG. 10. September SSTAs (°C) from CFSv2 forecasts with initial conditions in August–September 2019 (see section 2). Shown are results for the average of ensemble members that predict relatively (a) strong and (b) weak pIODs. The strong and weak categories are selected as the 90th and 10th percentile of the simulated October DMI, respectively (see Fig. 9i). (c) Differences between (a) and (b) that are statistically significant at the 90% confidence level.

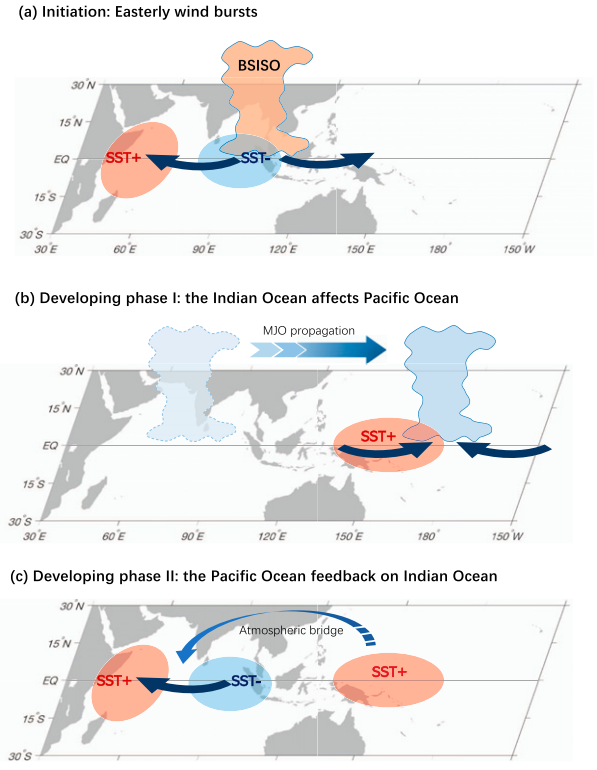

FIG. 11. Schematic diagram of the formation of the 2019 extreme pIOD. (a) At the initiation stage, the pIOD is triggered by an easterly wind burst associated with a dry phase of the BSISO. (b) In the developing phase I (the Indian Ocean affects the Pacific Ocean), the MJO that was initiated in the tropical Indian Ocean propagates eastward into the tropical Pacific, causing westerly wind anomalies in the central tropical Pacific. (c) In developing phase II (the Pacific Ocean feedbacks on the Indian Ocean), the westerly wind anomalies lead to positive SSTAs in the central tropical Pacific, which in turn enhances the easterly wind anomalies over the equatorial Indian Ocean thorough the atmospheric bridge, contributing to the further amplification of the 2019 pIOD.

Doi et al. (2020b) recently suggested that their model could predict the development of the 2019 pIOD. The model predicted the pIOD peaking in September and decaying thereafter, whereas in the observations, the amplitude of the pIOD almost doubles from September to October. As discussed above, the developments of the 2019 pIOD and the central-western tropical Pacific warm SSTA involve active subseasonal activities, which make it predictable only in a short range (1–2 months). This is likely the reason why the CFSv2 could not predict the 2019 pIOD event, although it is capable of predicting the pIOD events reasonably well one to two seasons ahead (Zhu et al. 2015). Indeed, it has been suggested that the predictability of a pIOD event may vary case by case due to different involvement of subseasonal activity, such as the MJO (Zhu et al. 2015). This highlights the important role of multiple-time-scale and cross-basin interactions in the variability and predictability of the tropical climate, which deserves further attention in future climate research and prediction.

Acknowledgments. We appreciate the constructive comments and insightful suggestions from three reviewers. Authors L. Zhang and W. Han are supported by National Science Foundation (NSF) OCE 1658132, NASA OSTST NNX17AI63G, and NSF AGS 1935279.

Data availability statement. All observational data used in this study are available online. Atmosphere and ocean model results are also available online (https://scholar.colorado.edu/concern/datasets/xp68kh20j).

REFERENCES

Allan, R. J., C. J. C. Reason, J. A. Lindesay, and T. J. Ansell, 2003: Protracted ENSO episodes and their impacts in the Indian Ocean region. *Deep-Sea Res. II*, **50**, 2331–2347, https://doi.org/10.1016/S0967-0645(03)00059-6.

Annamalai, H., R. Murtugudde, J. Potemra, S. P. Xie, P. Liu, and B. Wang, 2003: Coupled dynamics over the Indian Ocean: Spring initiation of the zonal mode. *Deep-Sea Res. II*, **50**, 2305–2330, https://doi.org/10.1016/S0967-0645(03)00058-4.

——, S. P. Xie, J. P. McCreary, and R. Murtugudde, 2005: Impact of Indian Ocean sea surface temperature on developing El Niño. *J. Climate*, **18**, 302–319, https://doi.org/10.1175/JCLI-3268.1.

Ashok, K., and N. H. Saji, 2007: On the impacts of ENSO and Indian Ocean dipole events on sub-regional Indian summer monsoon rainfall. *Nat. Hazards*, **42**, 273–285, https://doi.org/10.1007/s11069-006-9091-0.

——, Z. Guan, N. H. Saji, and T. Yamagata, 2004: Individual and combined influences of ENSO and the Indian Ocean Dipole on the Indian summer monsoon. *J. Climate*, **17**, 3141–3155, https://doi.org/10.1175/1520-0442(2004)017<3141:IACIOE>2.0.CO;2.

Behera, S. K., and T. Yamagata, 2003: Influence of the Indian Ocean Dipole on the Southern Oscillation. *J. Meteor. Soc. Japan*, **81**, 169–177, https://doi.org/10.2151/jmsj.81.169.

——, R. Krishnan, and T. Yamagata, 1999: Unusual ocean–atmosphere conditions in the tropical Indian Ocean during 1994. *Geophys. Res. Lett.*, **26**, 3001–3004, https://doi.org/10.1029/1999GL010434.

Black, E., J. Slingo, and K. R. Sperber, 2003: An observational study of the relationship between excessively strong short rains in coastal East Africa and Indian Ocean SST. *Mon. Wea. Rev.*, **131**, 74–94, https://doi.org/10.1175/1520-0493(2003)131<0074:AOSOTR>2.0.CO;2.

Cai, W., T. Cowan, and A. Sullivan, 2009: Recent unprecedented skewness towards positive Indian Ocean Dipole occurrences and its impact on Australian rainfall. *Geophys. Res. Lett.*, **36**, L11705, https://doi.org/10.1029/2009GL037604.

——, P. van Rensch, T. Cowan, and H. H. Hendon, 2011: Teleconnection pathways of ENSO and the IOD and the mechanisms for impacts on Australian rainfall. *J. Climate*, **24**, 3910–3923, https://doi.org/10.1175/2011JCLI4129.1.

——, A. Santoso, G. Wang, E. Weller, L. Wu, K. Ashok, Y. Masumoto, and T. Yamagata, 2014: Increased frequency of extreme Indian Ocean dipole events due to greenhouse warming. *Nature*, **510**, 254–258, https://doi.org/10.1038/nature13327.

——, and Coauthors, 2019: Pantropical climate interactions. *Science*, **363**, eaav4236, https://doi.org/10.1126/science.aav4236.

Clark, C. O., P. J. Webster, and J. E. Cole, 2003: Interdecadal variability of the relationship between the Indian Ocean zonal mode and East African coastal rainfall anomalies. *J. Climate*, **16**, 548–554, https://doi.org/10.1175/1520-0442(2003)016<0548:IVOTRB>2.0.CO;2.

Doi, T., S. K. Behera, and T. Yamagata, 2020a: Wintertime impacts of the 2019 super IOD on East Asia. *Geophys. Res. Lett.*, **47**, e2020GL089456, https://doi.org/10.1029/2020GL089456.

——, ——, and ——, 2020b: Predictability of the super IOD event in 2019 and its link with El Niño Modoki. *Geophys. Res. Lett.*, **47**, e2019GL086713, https://doi.org/10.1029/2019GL086713.

Du, Y., Y. Zhang, L. Zhang, T. Tozuka, B. Ng, and W. Cai, 2020: Thermocline warming induced extreme Indian Ocean dipole in 2019. *Geophys. Res. Lett.*, **47**, e2020GL090079, https://doi.org/10.1029/2020GL090079.

Feng, M., and G. Meyers, 2003: Interannual variability in the tropical Indian Ocean: A two-year time-scale of Indian Ocean Dipole. *Deep-Sea Res. II*, **50**, 2263–2284, https://doi.org/10.1016/S0967-0645(03)00056-0.

Gadgil, S., P. V. Joseph, and N. V. Joshi, 1984: Ocean–atmosphere coupling over monsoon regions. *Nature*, **312**, 141–143, https://doi.org/10.1038/312141a0.

——, P. N. Vinayachandran, P. A. Francis, and S. Gadgil, 2004: Extremes of the Indian summer monsoon rainfall, ENSO and equatorial Indian Ocean oscillation. *Geophys. Res. Lett.*, **31**, L12213, https://doi.org/10.1029/2004GL019733.

Graham, N. E., and T. P. Barnett, 1987: Sea surface temperature, surface wind divergence, and convection over tropical oceans. *Science*, **238**, 657–659, https://doi.org/10.1126/science.238.4827.657.

Gualdi, S., E. Guilyardi, A. Navarra, S. Masina, and P. Delecluse, 2003: The interannual variability in the tropical Indian Ocean as simulated by a CGCM. *Climate Dyn.*, **20**, 567–582, https://doi.org/10.1007/s00382-002-0295-z.

Han, W., 2005: Origins and dynamics of the 90-day and 30–60-day variations in the equatorial Indian Ocean. *J. Phys. Oceanogr.*, **35**, 708–728, https://doi.org/10.1175/JPO2725.1.

——, T. Shinoda, L. L. Fu, and J. P. McCreary, 2006: Impact of atmospheric intraseasonal oscillations on the Indian Ocean dipole during the 1990s. *J. Phys. Oceanogr.*, **36**, 670–690, https://doi.org/10.1175/JPO2892.1.

——, and Coauthors, 2014: Intensification of decadal and multi-decadal sea level variability in the western tropical Pacific during recent decades. *Climate Dyn.*, **43**, 1357–1379, https://doi.org/10.1007/s00382-013-1951-1.

Hersbach, H., and Coauthors, 2019: Global reanalysis: Goodbye ERA-Interim, hello ERA5. *ECMWF Newsletter*, No. 159, ECMWF, Reading, United Kingdom, 17–24.

Horii, T., H. Hase, I. Ueki, and Y. Masumoto, 2008: Oceanic precondition and evolution of the 2006 Indian Ocean dipole. *Geophys. Res. Lett.*, **35**, L03607, https://doi.org/10.1029/2007GL032464.

Huang, B., and J. L. Kinter III, 2002: Interannual variability in the tropical Indian Ocean. *J. Geophys. Res.*, **107**, 3199, https://doi.org/10.1029/2001JC001278.

——, and J. Shukla, 2007a: Mechanisms for the interannual variability in the tropical Indian Ocean. Part I: The role of remote forcing from the tropical Pacific. *J. Climate*, **20**, 2917–2936, https://doi.org/10.1175/JCLI4151.1.

——, and ——, 2007b: Mechanisms for the interannual variability in the tropical Indian Ocean. Part II: Regional processes. *J. Climate*, **20**, 2937–2960, https://doi.org/10.1175/JCLI4169.1.

——, Y. Xue, D. Zhang, A. Kumar, and M. J. McPhaden, 2010: The NCEP GODAS Ocean analysis of the tropical Pacific mixed layer heat budget on seasonal to interannual time scales. *J. Climate*, **23**, 4901–4925, https://doi.org/10.1175/2010JCLI3373.1.

——, and Coauthors, 2017: Extended reconstructed sea surface temperature, version 5 (ERSSTv5): Upgrades, validations, and intercomparisons. *J. Climate*, **30**, 8179–8205, https://doi.org/10.1175/JCLI-D-16-0836.1.

Izumo, T., and Coauthors, 2010: Influence of the state of the Indian Ocean Dipole on the following years El Niño. *Nat. Geosci.*, **3**, 168–172, https://doi.org/10.1038/ngeo760.

Ji, M., D. W. Behringer, and A. Leetmaa, 1998: An improved coupled model for ENSO prediction and implications for ocean initialization. Part II: The coupled model. *Mon. Wea. Rev.*, **126**, 1022–1034, https://doi.org/10.1175/1520-0493(1998)126<1022:AICMFE>2.0.CO;2.

Kiladis, G. N., J. Dias, K. H. Straub, M. C. Wheeler, S. N. Tulich, K. Kikuchi, K. M. Weickmann, and M. J. Ventrice, 2014: A comparison of OLR and circulation-based indices for tracking the MJO. *Mon. Wea. Rev.*, **142**, 1697–1715, https://doi.org/10.1175/MWR-D-13-00301.1.

Kripalani, R. H., and P. Kumar, 2004: Northeast monsoon rainfall variability over south peninsular India vis-à-vis the Indian Ocean dipole mode. *Int. J. Climatol.*, **24**, 1267–1282, https://doi.org/10.1002/joc.1071.

Krishnamurthy, V., and B. P. Kirtman, 2003: Variability of the Indian Ocean: Relation to monsoon and ENSO. *Quart. J. Roy. Meteor. Soc.*, **129**, 1623–1646, https://doi.org/10.1256/qj.01.166.

Lau, N. C., and M. J. Nath, 2004: Coupled GCM simulation of atmosphere–ocean variability associated with zonally asymmetric

SST changes in the tropical Indian Ocean. *J. Climate*, **17**, 245–265, https://doi.org/10.1175/1520-0442(2004)017<0245:CGSOAV>2.0.CO;2.

Lawrence, D. M., and P. J. Webster, 2002: The boreal summer intraseasonal oscillation: Relationship between northward and eastward movement of convection. *J. Atmos. Sci.*, **59**, 1593–1606, https://doi.org/10.1175/1520-0469(2002)059<1593:TBSIOR>2.0.CO;2.

Li, T., B. Wang, C.-P. Chang, and Y. Zhang, 2003: A theory for the Indian Ocean dipole–zonal mode. *J. Atmos. Sci.*, **60**, 2119–2135, https://doi.org/10.1175/1520-0469(2003)060<2119:ATFTIO>2.0.CO;2.

Li, Z., W. Cai, and X. Lin, 2016: Dynamics of changing impacts of tropical Indo-Pacific variability on Indian and Australian rainfall. *Sci. Rep.*, **6**, 31767, https://doi.org/10.1038/srep31767.

Liebmann, B., and C. A. Smith, 1996: Description of a complete (interpolated) outgoing longwave radiation dataset. *Bull. Amer. Meteor. Soc.*, **77**, 1275–1277.

Lim, Y., S.-W. Son, and D. Kim, 2018: MJO prediction skill of the subseasonal-to-seasonal prediction models. *J. Climate*, **31**, 4075–4094, https://doi.org/10.1175/JCLI-D-17-0545.1.

Lindzen, R. S., and S. Nigam, 1987: On the role of sea surface temperature gradients in forcing low-level winds and convergence in the tropics. *J. Atmos. Sci.*, **44**, 2418–2436, https://doi.org/10.1175/1520-0469(1987)044<2418:OTROSS>2.0.CO;2.

Lu, B., and H. Ren, 2020: What caused the extreme Indian Ocean Dipole event in 2019? *Geophys. Res. Lett.*, **47**, e2020GL087768, https://doi.org/10.1029/2020GL087768.

Luo, J.-J., R. Zhang, S. K. Behera, Y. Masumoto, F.-F. Jin, R. Lukas, and T. Yamagata, 2010: Interaction between El Niño and extreme Indian Ocean dipole. *J. Climate*, **23**, 726–742, https://doi.org/10.1175/2009JCLI3104.1.

——, W. Sasaki, and Y. Masumoto, 2012: Indian Ocean warming modulates Pacific climate change. *Proc. Natl. Acad. Sci. USA*, **109**, 18 701–18 706, https://doi.org/10.1073/pnas.1210239109.

Ma, S., C. Zhu, and J. Liu, 2020: Combined impacts of warm central equatorial Pacific sea surface temperatures and anthropogenic warming on the 2019 severe drought in East China. *Adv. Atmos. Sci.*, **37**, 1149–1163, https://doi.org/10.1007/s00376-020-0077-8.

Madden, R. A., and P. R. Julian, 1971: Detection of a 40–50 day oscillation in the zonal wind in the tropical Pacific. *J. Atmos. Sci.*, **28**, 702–708, https://doi.org/10.1175/1520-0469(1971)028<0702:DOADOI>2.0.CO;2.

McCreary, J. P., 1981: A linear stratified ocean model of the coastal undercurrent. *Philos. Trans. Roy. Soc. London*, **302A**, 385–413, https://doi.org/10.1098/rsta.1981.0176.

McPhaden, M. J., S. E. Zebiak, and M. H. Glantz, 2006: ENSO as an integrating concept in Earth science. *Science*, **314**, 1740–1745, https://doi.org/10.1126/science.1132588.

Meyers, G., P. McIntosh, L. Pigot, and M. Pook, 2007: The years of El Niño, La Niña and interactions with the tropical Indian Ocean. *J. Climate*, **20**, 2872–2880, https://doi.org/10.1175/JCLI4152.1.

Murtugudde, R., J. P. McCreary, and A. J. Busalacchi, 2000: Oceanic processes associated with anomalous events in the Indian Ocean with relevance to 1997–1998. *J. Geophys. Res.*, **105**, 3295–3306, https://doi.org/10.1029/1999JC900294.

Rao, S. A., and T. Yamagata, 2004: Abrupt termination of Indian Ocean dipole events in response to intraseasonal disturbances. *Geophys. Res. Lett.*, **31**, L19306, https://doi.org/10.1029/2004GL020842.

Rayner, N. A., D. E. Parker, E. B. Horton, C. K. Folland, L. V. Alexander, D. P. Rowell, E. C. Kent, and A. Kaplan, 2003: Global analyses of sea surface temperature, sea ice, and night marine air temperature since the late nineteenth century. *J. Geophys. Res.*, **108**, 4407, https://doi.org/10.1029/2002JD002670.

Reynolds, R. W., N. A. Rayner, T. M. Smith, D. C. Stokes, and W. Wang, 2002: An improved in situ and satellite SST analysis for climate. *J. Climate*, **15**, 1609–1625, https://doi.org/10.1175/1520-0442(2002)015<1609:AIISAS>2.0.CO;2.

Roeckner, E., and Coauthors, 1996: The atmospheric general circulation model ECHAM-4: Model description and simulation of present-day climate. Max-Planck-Institut für Meteorologie Doc., 171 pp.

Saha, S., and Coauthors, 2014: The NCEP Climate Forecast System version 2. *J. Climate*, **27**, 2185–2208, https://doi.org/10.1175/JCLI-D-12-00823.1.

Saji, N. H., and T. Yamagata, 2003: Possible impacts of Indian Ocean Dipole mode events on global climate. *Climate Res.*, **25**, 151–169, https://doi.org/10.3354/cr025151.

——, B. N. Goswami, P. N. Vinayachandran, and T. Yamagata, 1999: A dipole mode in the tropical Indian Ocean. *Nature*, **401**, 360–363, https://doi.org/10.1038/43854.

——, S. P. Xie, and T. Yamagata, 2006: Tropical Indian Ocean variability in the IPCC twentieth-century climate simulations. *J. Climate*, **19**, 4397–4417, https://doi.org/10.1175/JCLI3847.1.

Shinoda, T., H. H. Hendon, and M. A. Alexander, 2004: Surface and subsurface dipole variability in the Indian Ocean and its relation with ENSO. *Deep-Sea Res. I*, **51**, 619–635, https://doi.org/10.1016/j.dsr.2004.01.005.

Stuecker, M. F., A. Timmermann, F. F. Jin, Y. Chikamoto, W. Zhang, A. T. Wittenberg, E. Widiasih, and S. Zhao, 2017: Revisiting ENSO/Indian Ocean Dipole phase relationships. *Geophys. Res. Lett.*, **44**, 2481–2492, https://doi.org/10.1002/2016GL072308.

Vinayachandran, P. N., N. H. Saji, and T. Yamagata, 1999: Response of the equatorial Indian Ocean to an unusual wind event during 1994. *Geophys. Res. Lett.*, **26**, 1613–1616, https://doi.org/10.1029/1999GL900179.

Waliser, D. E., and N. E. Graham, 1993: Convective cloud systems and warm-pool sea surface temperatures: Coupled interactions and self-regulation. *J. Geophys. Res.*, **98**, 12 881–12 893, https://doi.org/10.1029/93JD00872.

Wang, C., 2019: Three-ocean interactions and climate variability: A review and perspective. *Climate Dyn.*, **53**, 5119–5136, https://doi.org/10.1007/s00382-019-04930-x.

Wang, G., W. Cai, K. Yang, A. Santoso, and T. Yamagata, 2020: A unique feature of the 2019 extreme positive Indian Ocean Dipole event. *Geophys. Res. Lett.*, **47**, e2020GL088615, https://doi.org/10.1029/2020GL088615.

Wang, H., A. Kumar, R. Murtugudde, B. Narapusetty, and K. L. Seip, 2019: Covariations between the Indian Ocean dipole and ENSO: A modeling study. *Climate Dyn.*, **53**, 5743–5761, https://doi.org/10.1007/s00382-019-04895-x.

Webster, P. J., A. M. Moore, J. P. Loschnigg, and R. R. Leben, 1999: Coupled ocean–atmosphere dynamics in the Indian Ocean during 1997–98. *Nature*, **401**, 356–360, https://doi.org/10.1038/43848.

Xue, Y., M. Chen, A. Kumar, Z.-Z. Hu, and W. Wang, 2013: Prediction skill and bias of tropical Pacific sea surface temperatures in the NCEP Climate Forecast System version 2. *J. Climate*, **26**, 5358–5378, https://doi.org/10.1175/JCLI-D-12-00600.1.

Yu, J. Y., Y. Zou, S. T. Kim, and T. Lee, 2012: The changing impact of El Niño on US winter temperatures. *Geophys. Res. Lett.*, **39**, L15702, https://doi.org/10.1029/2012GL052483.

Zhang, L., and W. Han, 2018: Impact of Ningaloo Niño on tropical Pacific and an interbasin coupling mechanism. *Geophys. Res. Lett.*, **45**, 11 300–11 309, https://doi.org/10.1029/2018GL078579.

——, ——, K. B. Karnauskas, G. A. Meehl, A. Hu, N. Rosenbloom, and T. Shinoda, 2019: Indian Ocean warming trend reduces Pacific warming response to anthropogenic greenhouse gases: An interbasin thermostat mechanism. *Geophys. Res. Lett.*, **46**, 10 882–10 890, https://doi.org/10.1029/2019GL084088.

Zhu, J., B. Huang, A. Kumar, and J. L. Kinter III, 2015: Seasonality in prediction skill and predictable pattern of tropical Indian Ocean SST. *J. Climate*, **28**, 7962–7984, https://doi.org/10.1175/JCLI-D-15-0067.1.